

## A chip-scale RF MEMS gyrator via hybridizing Lorentz-force and piezoelectric transductions

Wu, Tao; Lu, Ruochen; Gao, Anming; Tu, Cheng; Manzanque, Tomas; Gong, Songbin

**DOI**

[10.1109/MEMSYS.2019.8870764](https://doi.org/10.1109/MEMSYS.2019.8870764)

**Publication date**

2019

**Document Version**

Final published version

**Published in**

Proceedings of the IEEE 32nd International Conference on Micro Electro Mechanical Systems (MEMS 2019)

**Citation (APA)**

Wu, T., Lu, R., Gao, A., Tu, C., Manzanque, T., & Gong, S. (2019). A chip-scale RF MEMS gyrator via hybridizing Lorentz-force and piezoelectric transductions. In *Proceedings of the IEEE 32nd International Conference on Micro Electro Mechanical Systems (MEMS 2019)* (pp. 887-890). IEEE.  
<https://doi.org/10.1109/MEMSYS.2019.8870764>

**Important note**

To cite this publication, please use the final published version (if applicable).  
Please check the document version above.

**Copyright**

Other than for strictly personal use, it is not permitted to download, forward or distribute the text or part of it, without the consent of the author(s) and/or copyright holder(s), unless the work is under an open content license such as Creative Commons.

**Takedown policy**

Please contact us and provide details if you believe this document breaches copyrights.  
We will remove access to the work immediately and investigate your claim.

# A CHIP-SCALE RF MEMS GYRATOR VIA HYBRIDIZING LORENTZ-FORCE AND PIEZOELECTRIC TRANSDUCTIONS

Tao Wu<sup>1</sup>, Ruochen Lu<sup>2</sup>, Anming Gao<sup>2</sup>, Cheng Tu<sup>3</sup>, Tomás Manzanque<sup>4</sup>, and Songbin Gong<sup>2</sup>

<sup>1</sup>ShanghaiTech University, Shanghai, China

<sup>2</sup>University of Illinois at Urbana-Champaign, Urbana, IL, USA

<sup>3</sup>Northeastern University, Boston, MA, USA

<sup>4</sup>Delft University of Technology, Delft, Netherlands

## ABSTRACT

This paper presents the design and experimental results of the first chip-scale radio frequency MEMS gyrator based on hybridizing Lorentz-force and piezoelectric transduction. The MEMS gyrator has a non-reciprocal phase response of  $180^\circ$  and can be used as the building blocks for synthesizing complex non-reciprocal networks. The equivalent circuit and measured performance of a fabricated MEMS gyrator are presented, both showing the anticipated  $180^\circ$  phase difference. The demonstration marks the first time that non-reciprocity is attained at radio frequencies with an entirely passive chip-scale mechanical device. Various challenges in achieving strong coupling and low insertion loss for the designed devices will be discussed.

## INTRODUCTION

Radio frequency (RF) non-reciprocal networks (e.g., circulators) are critical enablers for full-duplex radios that can simultaneously transmit and receive over the same bandwidth. Conventionally, the implementation of nonreciprocal devices at RF typically resort to magnetic-field biased ferrite devices, which require magnets and are difficult to integrate on-chip. They also operate exclusively in the electromagnetic (EM) domain and have sizes comparable to large EM wavelengths at RF. To overcome the disadvantages of conventional ferrite devices, two promising approaches have been explored recently. The first approach relies on time-varying circuits to attain non-reciprocity on chip-scale while eliminating the need for magnetic biasing [1-6]. The second approach turns to ferrite-cored lumped elements and a thin-profile magnet embedded in packaging to achieve  $>50x$  size reduction [7]. Despite the significant advances in size reduction demonstrated in both approaches, the time-varying approach requires  $>100$  mW power consumption in implementation while the lumped element ferrite devices are still not yet integration-compatible with CMOS on chip scale. To drastically reduce the sizes of non-reciprocal devices while consuming zero power, the acoustic or mechanical domain can be leveraged as acoustic wavelengths are four to five orders of magnitude smaller than their EM counterparts [8].

Inspired by the original prediction of McMillan [9] and Tellegen [10] that non-reciprocity can be realized by the gyroscopic magneto-electric transduction mediated via the mechanical domain, this work explores a MEMS anti-reciprocal system (e.g., gyrator) that relies on the same principle of coupling the piezoelectric and electrodynamic transductions [9]. The magneto-electric transduction is achieved herein by utilizing Lorentz-force and piezoelectric transductions in tandem in a single structure. In comparison to other attempts to harnesses the voltage-current

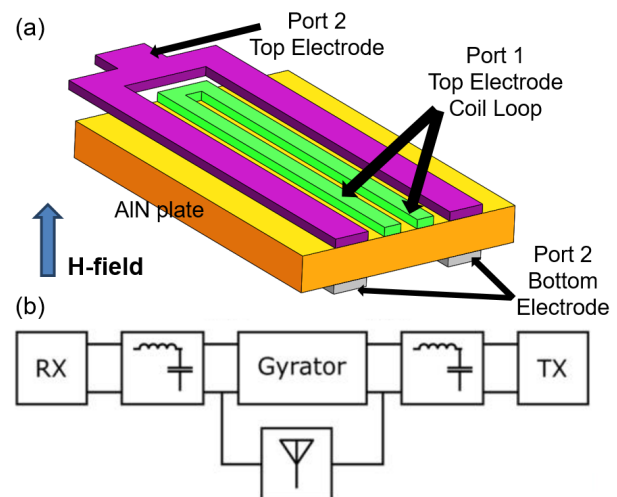


**Figure 1:** (a) Proposed chip-scale electromechanical gyrator; (b) 3-port circulator constructed from the gyrator and matching networks and connected to a transmitter (TX), receiver (RX), and antenna in a full-duplex scenario.

gyration in the magneto-electric transduction at the kHz range [11-13], our design does not employ any magnetic material in the transduction and thus can be miniaturized and integrated on-chip to scale towards GHz. As a result of this novel concept, this work demonstrates the first chip-scale resonant magneto-electric MEMS gyrator at RF, suggesting a promising alternative for accomplishing chip-scale non-reciprocity.

## DESIGN AND MODELING

Fig. 1(a) shows the schematic of our proposed gyrator, which consists of a rectangular AlN thin plate with carefully designed electrodes serving as the electrodynamic port (Port 1) and the piezoelectric port (Port 2), respectively. In operation, the two-port gyrator can be either piezoelectrically driven via the interdigitated electrodes or magnetically excited via the coil by Lorentz-force. In the forward path, the applied AC voltage across the coil (Port 1) would generate a magnetic force under the external magnetic field (i.e., Lorentz Force), exciting the AlN structure into the vibration of a higher order extensional mode. As the strain produced by the Lorentz-Force couples across the piezoelectric material, it converts to a voltage across Port 2 via piezoelectric transduction with a  $90^\circ$  phase delay from the voltage across Port 1. In the backward path, the voltage applied to Port 2 piezoelectrically excites the structure into the lateral vibration of the same mode, the energy of which is converted to a current in the coil via Faraday's law of induction, yielding a voltage  $90^\circ$  leading the voltage across Port 2. Consequently, between the forward and backward

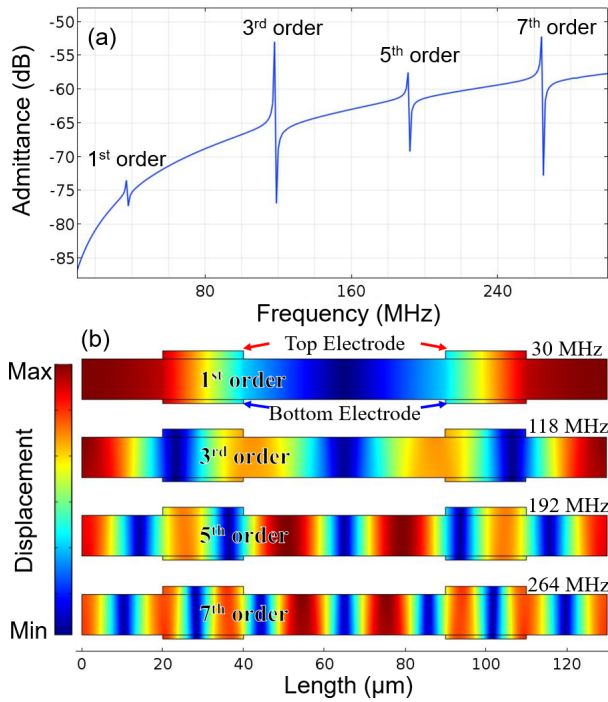


**Figure 2:** (a) Simulated admittance of a 200  $\mu\text{m}$  long by 130  $\mu\text{m}$  wide by 1  $\mu\text{m}$  thick AlN plate excited by two pairs of 100 nm Pt bottom electrode and 200 nm Al top electrode; and (b) cross-sectional view of four resonant mode shapes at 30 MHz, 118 MHz, 192 MHz and 264 MHz, respectively.

paths is a nonreciprocal phase difference of  $180^\circ$ . In such a design, the suspended composite structure essentially serves as a resonance-enhanced magneto-electric transducer that hybridizes the Lorentz-Force and piezoelectric transduction and behaves like a gyator.

Such a chip-scale MEMS gyator, similar to other implementations of a gyator, can serve as a building block to construct multi-port nonreciprocal networks (e.g., circulators) [3]. For instance, an electromechanical circulator can be built based on the resonant gyator via a typical topology to provide clockwise circulation as shown in Fig. 1(b) [12]. Because the piezoelectric and electrodynamic transductions have different coupling efficiencies, impedance matching networks are required at two of the circulator ports. In the rest of this section, we will discuss the gyator by co-designing piezoelectric and Lorentz-force transductions and then analyzing the gyator performance via an equivalent circuit model.

As seen in Fig. 1(a), the piezoelectric portion of the device resembles a conventional laterally vibrating AlN resonator (LVR), which usually consists of an AlN thin film sandwiched by top and bottom electrodes [14, 15]. A coil loop is essential to implementing the electrodynamic transduction and should be routed on either the top or bottom side of the AlN thin film. Similar to a conventional AlN LVR, the top and bottom electrodes of the piezoelectric transducer should be centered at nodal points of the intended resonant mode, while the coil should be positioned where maximum displacement occurs at resonance. To this end, a COMSOL 2D-simulation is first utilized to analyze the resonant modes of the AlN plate for optimizing piezoelectric and Lorentz-Force transductions. Fig. 2 (a)

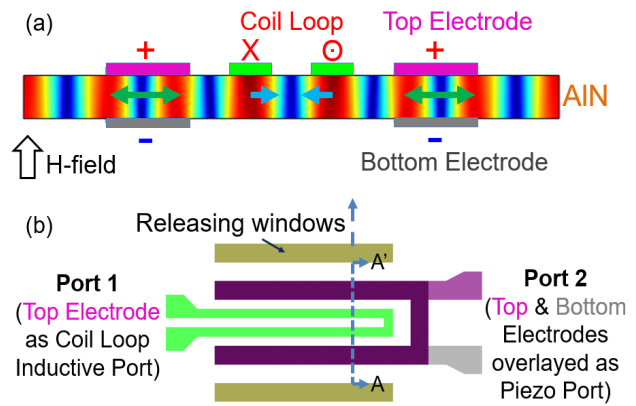


**Figure 3:** (a) Simulated cross-sectional view ( $A-A'$ ) of the AlN gyator displacement mode shape at resonance. (b) Layout view of the designed MEMS Gyator.

shows the admittance response of a 1  $\mu\text{m}$  thick AlN plate (200  $\mu\text{m}$  by 130  $\mu\text{m}$ ) excited by two pairs of top and bottom electrodes with 50  $\mu\text{m}$  separation. Four pronounced resonances are clearly observed in the plot, corresponding to the 1<sup>st</sup>, 3<sup>rd</sup>, 5<sup>th</sup>, and 7<sup>th</sup> order S0 modes. Their mode shapes are plotted in Fig. 2(b). Considering that the S0 mode is only weakly dispersive, the resonances are collectively set by the device width ( $W$ ) and the mode order ( $N$ ):

$$f_0^N \approx \frac{N v_{s0}}{2W} \quad (1)$$

where  $v_{s0}$  is the phase velocity of the S0 mode. Only odd-order modes are excited in this configuration. To achieve the earlier-mentioned aim of placing piezoelectric transducers at nodal points and electrodynamic transducers at nodes of maximum displacement for maximum magneto-electric coupling, we choose the 7<sup>th</sup> order mode for gyator operation. As shown in Fig. 3(a), the coil loop can be then properly aligned to the center red regions where maximum strain and displacement occur. The coil electrode is slightly narrower compared to the electrodes for piezoelectric transduction due to these considerations. The widths of the top and bottom electrodes of the piezoelectric transducer are set to 20  $\mu\text{m}$  with a lateral spacing of 50  $\mu\text{m}$  while the U-shaped single-turn coil is set to 10  $\mu\text{m}$  wide with a 10  $\mu\text{m}$  spacing between the two parallel segments of the coil. This configuration matches the 7<sup>th</sup> order mode shape and maximizes both the piezoelectric and electrodynamic transduction. Fig. 3(b) illustrates the designed gyator layout. We choose 100 nm Pt as the bottom electrode, 1  $\mu\text{m}$  of AlN as the piezoelectric layer, and 200 nm Al as the top electrode for the piezoelectric transducer as well as the coil. In comparison to other EM gyators, our design enables a drastic reduction in the gyator size, while allowing the coupling to be independently controlled through an external magnetic bias field.

Fig. 4 shows the equivalent circuit model and the simulation results of the designed MEMS gyator.  $C_m$ ,  $L_m$ , and  $R_m$  are the equivalent spring, mass, and damper in the mechanical domain. The ideal gyator model with a coupling coefficient of  $\eta_{LF}$  is used to capture the Lorentz-Force transduction, while the ideal transformer model with a coupling coefficient of  $\eta_{PE}$  is adopted to represent the piezoelectric transduction.  $L_{coil}$  and  $R_{coil}$  represent the inductance

Table 1: Parameters of the equivalent circuit model.

Parameter	$C_m$ (m/N)	$L_m$ (kg)	$R_m$ (kg/s)	$L_{coil}$ (nH)	$R_{coil}$ ( $\Omega$ )	$C_0$ (pF)	$B$ (T)	$e_{31}$ (C/m <sup>2</sup> )	$\eta_{LF}$ (Vs/m)	$\eta_{PE}$ (sA/m)
Value	$54.1 \cdot 10^{-9}$	$6.86 \cdot 10^{-12}$	$1.04 \cdot 10^{-5}$	0.6	15.3	0.67	0.28	0.6	$5.6 \cdot 10^{-5}$	$2.4 \cdot 10^{-4}$

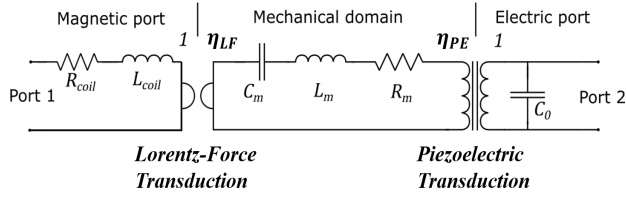


Figure 4: Equivalent circuit model for the designed MEMS gyrotor.

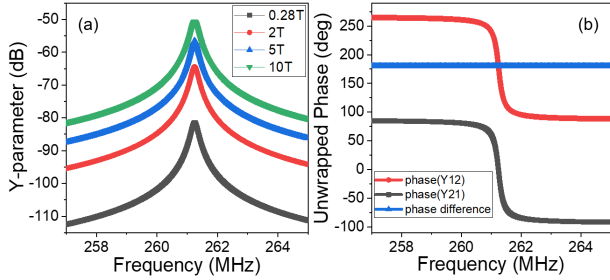


Figure 5: (a) Simulated  $Y_{21}$  at different magnetic field biases of 0.28 T, 2 T, 5 T and 10 T. (b) Simulated phases of  $Y_{12}$ ,  $Y_{21}$  and their phase difference at the magnetic field bias of 0.28 T.

and resistance of the top coil, respectively, while  $C_0$  denotes the static capacitance formed by the electrodes sandwiching the piezoelectric film. Matching networks can be used to match the input and output ports to 50  $\Omega$ .

For the Lorentz-Force transduction, the magnitude the Lorentz-Force can be expressed as:

$$F_{LF} = I_{coil} L \times B \quad (2)$$

where  $I_{coil}$  is the current flowing through the gyrotor coil,  $B$  is the magnetic flux density, and  $L$  is the longitudinal length of the coil. Therefore, the Lorentz-Force coupling coefficient of  $\eta_{LF}$  can be derived from:

$$\eta_{LF} = \frac{F_{LF}}{I_{coil}} = L \times B \quad (3)$$

The piezoelectric coupling coefficient  $\eta_{PE}$  can be correlated with the piezoelectric coefficient ( $e_{31}$ ) for thickness field excitation as:

$$\eta_{PE} = \frac{F_{PE}}{V_{PE}} = 2e_{31}L \quad (4)$$

where  $L$  is the electrode length, which is the same as the longitudinal length of the coil. The parameters used in the circuit model are extracted from the FEM simulation results, which are listed and summarized in the Table 1.

With the circuit model and extracted parameters, the performance of the gyrotor under different external magnetic bias can be evaluated. Fig. 5(a) plots the simulated two-port admittance ( $Y_{12}$  and  $Y_{21}$ ) in magnitude dB at different magnetic field biases of 0.28 T, 2 T, 5 T, and 10 T. Since the magnitudes of  $Y_{21}$  and  $Y_{12}$  are the same, we only plot  $Y_{21}$  in Fig. 5(a). It is expected that the gyration performance can be improved with a more considerable external magnetic field bias, as a larger magnetic bias  $B$  will increase the Lorentz-force coupling,  $\eta_{LF}$ . Fig. 5(b) plots the simulated phase responses of  $Y_{12}$  and  $Y_{21}$  and the phase

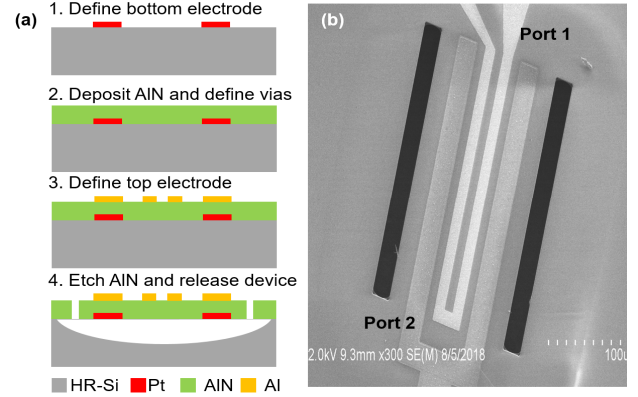


Figure 6: (a) Fabrication process. (b) SEM of a fabricated gyrotor. Port 1 is the inductive coil loop for Lorentz-force transduction, and Port 2 consists of 2 pairs of top and bottom electrodes for piezoelectric transduction.

difference between them at a magnetic field bias of 0.28 T. An anticipated, a non-reciprocal phase difference of 180° is seen in the simulation results.

## FABRICATION AND MEASUREMENTS

The device was fabricated with a simple four-mask process as shown in Fig. 6. First, a 100 nm Pt layer is deposited on a high-resistive Si substrate using a lift-off process to form the bottom electrode connected to Port 2 [Fig. 6(a)]. Then, a 1  $\mu$ m AlN is sputtered, and vias are patterned using wet-etching to access the bottom electrodes. A 200 nm Al layer is subsequently deposited and patterned on top of the AlN layer as the top electrode connected to Port 2 and the coil connected to Port 1. Finally, after the release windows are defined with a  $Cl_2/BCl_3$ -based reactive ion etching process, the gyrotor is released with the  $XeF_2$  isotropic dry etching. Fig. 6(b) shows the SEM image of a fabricated gyrotor device with the dimensions of 130  $\mu$ m by 200  $\mu$ m. The top electrodes of both ports are identified in the figure. The suspended structure is fully anchored on two ends.

To test the gyrotor, the fabricated device is placed on a customized probe station made of non-magnetic materials. A permanent magnet is positioned right underneath the device at an adjustable height. The magnetic field bias applied to the device can be changed by adjusting the distance between the permanent magnet and device. The maximum magnetic field available in our measurement is 2800 Oe or 0.28 T. Non-magnetic GSG RF probes and a Vector Network Analyzer (VNA) were used to characterize the two-port S-parameters of the gyrotor.

Fig. 7 plots the measured results of Y-parameters in magnitude (dB) and phases (degree). Thanks to the resonance-enhancement of non-reciprocity, the fabricated device exhibits voltage current gyration near 261.42 MHz under a magnetic field of 0.28 T. As seen in the simulation,  $Y_{12}$  and  $Y_{21}$  display nearly the same magnitude [Fig. 7(a)] and a 180° difference between the forward and backward

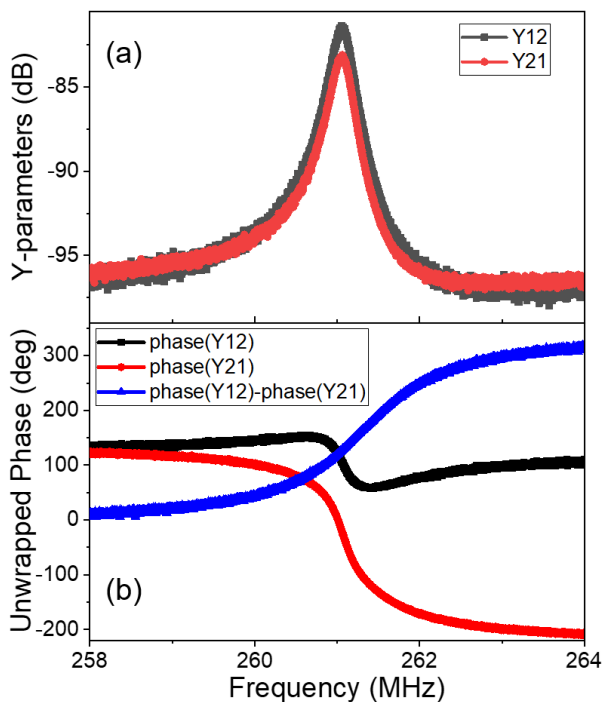


**Figure 7:** Characterized MEMS gyrator Y-parameter in (a) magnitude (dB) and (b) phases (degree) at the maximum applied external magnetic field bias of 0.28T.

paths [Fig. 7 (b)]. Experimental data also shows that the amplitude increases with an increasing magnetic field bias and reaches the maximum at the maximum available bias of 0.28 T in our setup. Other factors limiting the transduction efficiency are the resistive loss such as coil and routing resistance, and low piezoelectric coupling coefficients  $\eta_{PE}$  in AlN. Other piezoelectric materials with a larger coupling coefficient, such as LiNbO<sub>3</sub>, could be leverage to further improve the gyration efficiency [16-19]. As shown in Fig. 7(b), the phase difference between Y<sub>21</sub> and Y<sub>12</sub> varies verse frequency and the 180° phase non-reciprocity can only be maintained over a narrow bandwidth. This could attribute to another reciprocal path between the two ports, such as the capacitive coupling between piezoelectric top electrodes and inductive coil loop.

## CONCLUSIONS

We have demonstrated a chip-scale RF MEMS gyrator based on combining Lorentz-Force and Piezoelectric transduction mechanisms. The nonreciprocal 180° phase difference occurs at approximately 261.42 MHz due to the resonance-enhanced Lorentz-Force gyroscopic transduction. Upon further improvement in transduction efficiency and loss, such a MEMS gyrator could potentially be used as the building blocks for synthesizing complex non-reciprocal networks and enabling a full micro-electro-mechanical RF front-end system.

## REFERENCES

[1] M. M. Biedka, R. Zhu, Q. M. Xu, and Y. E. Wang, "Ultra-wide band non-reciprocity through sequentially-switched delay lines." *Scientific reports* 7 (2017): 40014.  
 [2] A. Kord, D. L. Sounas, and A. Alù, "Pseudo-Linear Time-Invariant Magnetless Circulators Based on Differential Spatiotemporal Modulation of Resonant Junctions," *IEEE*

*Trans. Microw. Theory Techn.*, vol. 66, no. 6, pp. 2731-2745, 2018.  
 [3] N. Reiskarimian and H. Krishnaswamy, "Magnetic-free non-reciprocity based on staggered commutation," *Nature communications*, vol. 7, p. 11217, 2016.  
 [4] R. Lu, J. Krol, L. Gao, and S. Gong. "A Frequency Independent Framework for Synthesis of Programmable Non-reciprocal Networks." *Scientific reports* 8 (2018): 14655.  
 [5] R. Lu, T. Manzanque, Y. Yang, L. Gao, A. Gao, and S. Gong. "A Radio Frequency Non-reciprocal Network Based on Switched Acoustic Delay Lines." *arXiv preprint arXiv:1803.10665* (2018).  
 [6] Y. Yu *et al.*, "Magnetic-free radio frequency circulator based on spatiotemporal commutation of MEMS resonators," *2018 IEEE Micro Electro Mechanical Systems (MEMS)*, Belfast, 2018, pp. 154-157.  
 [7] T. Wada *et al.*, "A miniaturized broadband lumped element circulator for reconfigurable front-end system," pp. 1-3: *IEEE*.  
 [8] S. Gong, R. Lu, T. Manzanque, C. Tu, D. Shoemaker, and C. Zhao, University of Illinois, 2018. Chip-scale resonant gyrator for passive non-reciprocal devices. U.S. Patent Application 15/790,999.  
 [9] E. M. McMillan, "Violation of the reciprocity theorem in linear passive electromechanical systems," *The Journal of the Acoustical Society of America*, vol. 18, no. 2, pp. 344-347, 1946.  
 [10] B. D. Tellegen, "The gyrator, a new electric network element," *Philips Res. Rep.*, vol. 3, no. 2, pp. 81-101, 1948.  
 [11] H. Gamo, "On passive one-way systems," *IRE Transactions on Circuit Theory*, vol. 6, no. 5, pp. 283-298, 1959.  
 [12] J. Silverman, "The Electromechanical Circulator," *IRE Transactions on Component Parts*, vol. 9, no. 2, pp. 81-85, 1962.  
 [13] J. Zhai, J. Li, S. Dong, D. Viehland, and M. I. Bichurin, "A quasi (unidirectional) Tellegen gyrator," *Journal of applied physics*, vol. 100, no. 12, p. 124509, 2006.  
 [14] G. Piazza, P. J. Stephanou, and A. P. Pisano, "Piezoelectric aluminum nitride vibrating contour-mode MEMS resonators," *Departmental Papers (ESE)*, p. 223, 2006.  
 [15] M. Rinaldi, C. Zuniga, C. Zuo, and G. Piazza, "Super-high-frequency two-port AlN contour-mode resonators for RF applications," *IEEE transactions on ultrasonics, ferroelectrics, and frequency control*, vol. 57, no. 1, 2010.  
 [16] S. Gong and G. Piazza, "Design and analysis of lithium-niobate-based high electromechanical coupling RF-MEMS resonators for wideband filtering," *IEEE Transactions on Microwave Theory and Techniques*, vol. 61, no. 1, pp. 403-414, 2013.  
 [17] S. Gong and G. Piazza, "Figure-of-merit enhancement for laterally vibrating lithium niobate MEMS resonators," *IEEE Transactions on Electron Devices*, vol. 60, no. 11, pp. 3888-3894, 2013.  
 [18] Y. Yang, R. Lu, T. Manzanque and S. Gong, "1.7 GHz Y-Cut Lithium Niobate MEMS Resonators with FoM of 336 and fQ of  $9.15 \times 10^{12}$ ," *2018 IEEE/MTT-S International Microwave Symposium - IMS*, Philadelphia, PA, 2018, pp. 563-566.  
 [19] L. Colombo, A. Kochhar, G. Vidal-Álvarez and G. Piazza, "X-Cut Lithium Niobate Laterally Vibrating MEMS Resonator With Figure of Merit of 1560," in *Journal of Microelectromechanical Systems*, vol. 27, no. 4, pp. 602-604, Aug. 2018.

## CONTACT

Tao Wu, [wutao@shanghaitech.edu.cn](mailto:wutao@shanghaitech.edu.cn)